



Article

Effects of Oxygen on Lattice Defects in Single-Crystalline Mg₂Si Thermoelectrics

Kei Hayashi ^{1,*}, Sota Kawamura ², Yusuke Hashimoto ², Noboru Akao ³, Zhicheng Huang ¹, Wataru Saito ¹, Kaichi Tasaki ¹, Koichi Hayashi ^{4,5}, Tomohiro Matsushita ² and Yuzuru Miyazaki ¹

¹ Department of Applied Physics, Graduate School of Engineering, Tohoku University, Sendai 980-8579, Japan

² Graduate School of Science and Technology, Nara Institute of Science and Technology, Ikoma 630-0192, Japan

³ Department of Materials Science, Graduate School of Engineering, Tohoku University, Sendai 980-8579, Japan

⁴ Department of Physical Science and Engineering, Nagoya Institute of Technology, Nagoya 466-8555, Japan

⁵ Japan Synchrotron Radiation Research Institute (JASRI), Sayo 679-5198, Japan

* Correspondence: kei.hayashi.b5@tohoku.ac.jp; Tel.: +81-22-795-4637

Abstract: Lattice defect engineering has attracted attention due to its ability to develop thermoelectric materials with low thermal conductivity. For Mg₂Si single crystals (SCs), Si vacancy (V_{Si}) defects can be introduced and consequently result in the formation of dislocation cores. These lattice defects confer Mg₂Si SCs with a lower thermal conductivity compared to Mg₂Si polycrystals. To reveal a mechanism for the stabilisation of V_{Si} in the Mg₂Si SCs, we investigated the effects of oxygen (O) on lattice defects by performing electronic structure calculations, secondary ion mass spectrometry, X-ray photoelectron spectroscopy, and photoelectron holography. On the basis of these calculations, we predicted that O stabilised the formation of V_{Si} when it was located at the Si site or at an interstitial site. All experiments confirmed the presence of O inside the Mg₂Si SCs. However, O was suggested to be located not at the specific site in the crystal lattice of Mg₂Si but at dislocation cores. The interaction between O and the dislocation cores in the Mg₂Si SC is expected to immobilise dislocation cores, leading to the stabilisation of V_{Si} formation.



Citation: Hayashi, K.; Kawamura, S.; Hashimoto, Y.; Akao, N.; Huang, Z.; Saito, W.; Tasaki, K.; Hayashi, K.; Matsushita, T.; Miyazaki, Y. Effects of Oxygen on Lattice Defects in Single-Crystalline Mg₂Si Thermoelectrics. *Nanomaterials* **2023**, *13*, 1222. <https://doi.org/10.3390/nano13071222>

Academic Editors: Lyubov G. Bulusheva and Zhanxi Fan

Received: 31 January 2023

Revised: 20 March 2023

Accepted: 24 March 2023

Published: 30 March 2023



Copyright: © 2023 by the authors. Licensee MDPI, Basel, Switzerland. This article is an open access article distributed under the terms and conditions of the Creative Commons Attribution (CC BY) license (<https://creativecommons.org/licenses/by/4.0/>).

Keywords: Mg₂Si single crystals; lattice defects; electronic structure calculations; photoelectron holography

1. Introduction

Lattice defect engineering is key to developing energy-harvesting materials such as photovoltaic, dielectric, and thermoelectric (TE) materials [1–3]. Lattice defects such as point defects and dislocation cores should be reduced in photovoltaic and dielectric materials to achieve high energy-conversion efficiency. Although the introduction of lattice defects into TE materials also affects TE properties (the Seebeck coefficient, electrical conductivity, and thermal conductivity) [4–31], it can improve TE performance mainly because lattice thermal conductivity (κ_L) decreases due to enhanced phonon scattering by lattice defects [5,11,16,19,23,24,29–31]. Thus, investigating which point defect is formed and how it works in TE materials is important.

In this study, we focused on Mg₂Si, which has attracted considerable attention as a potential TE material [3,8,21,32,33]. Mg₂Si has an antiferrotype structure (space group: $Fm\bar{3}m$), wherein the $8c(1/4\ 1/4\ 1/4)$ and the $4a(0\ 0\ 0)$ sites were occupied by Mg and Si, respectively. The most probable point of the defect in Mg₂Si was theoretically predicted to be an interstitial defect in which the $4b(1/2\ 1/2\ 1/2)$ site was partially occupied by Mg [34–36]. This interstitial Mg (Mg_i) was present in synthesised Mg₂Si-based polycrystals (PCs) [6,7,21,37]. However, recent studies have revealed that undoped and boron (B)-doped Mg₂Si single crystals (SCs) contain Si vacancy (V_{Si}) defects [17]. In addition, V_{Si} defects induce edge dislocation cores in these Mg₂Si-based SCs [27]. As a result of the presence of V_{Si} defects and dislocation cores, Mg₂Si-based SCs exhibited lower κ_L than Mg₂Si

PCs [27]. The difference in point defects between Mg₂Si-based PCs and SCs may arise from preparation temperature, which is typically 1123 K for Mg₂Si-based PCs [6,7] and 1413 K for Mg₂Si-based SCs [17,27]. The higher preparation temperature for Mg₂Si-based SCs can induce V_{Si}. However, Mg₂Si with V_{Si} is not expected to be stable, because V_{Si} has higher formation energy than Mg_i [34–36]. One possibility for the stabilisation of V_{Si} in Mg₂Si is its incorporation with oxygen (O). A theoretical study predicted that O intercalation into the 4b(1/2 1/2 1/2) site resulted in p-type Mg₂Si [38]. This prediction was consistent with the findings of an experimental study on postannealed Mg₂Si thin films [39], which also suggested that Mg vacancy (V_{Mg}) defects were formed through the postannealing process. The other possibility for interaction between dislocation cores and O. In a Si SC, O diffuses during preparation and precipitates at dislocation cores [40–43]. Subsequently, location of Si and O atoms were rearranged around dislocation cores, making the dislocation cores stable [41–43]. A similar O precipitation at the dislocation cores may occur in Mg₂Si-based SCs, leading to the stabilization of V_{Si}.

Motivated by the above studies, we investigated the effects of O on V_{Si} and the dislocation cores in Mg₂Si SCs. By using first-principles electronic structure calculations, we examined whether the incorporation of O stabilised the formation of V_{Si}. Furthermore, we performed secondary ion mass spectrometry (SIMS), X-ray photoelectron spectroscopy (XPS), and photoelectron holography to verify the existence of O in the prepared Mg₂Si SCs. In particular, on the basis of photoelectron holograms, we discussed the three-dimensional atomic arrangements of Mg, Si, and O.

2. Calculation and Experimental Methods

We used the full-potential linearised augmented plane wave (FLAPW) method implemented in the Wien2k code [44] and the Korringa-Kohn-Rostoker (KKR) method under the coherent potential approximation implemented in the AkaiKKR code [45] to reduce the cost for the electronic structure calculation. Although the GW approximation, using the Green's function G and the screened Coulomb potential W , has been reported to be the most accurate method for the calculation of Mg₂Si, Mg₂Ge, and Mg₂Sn [46], the FLAPW and/or KKR methods are known to be sufficient for determining the conduction type and comparing the total energy, E , of different crystal structure models [8,10,12,18–20,22,25,28]. The local exchange-correlation potential in generalised gradient approximation was used for calculation through the FLAPW method. Twelve crystal structure models with a $2 \times 2 \times 2$ cubic supercell were used, as shown in Figures S1–S3. Model 1 is 'Mg₆₄Si₃₂', which contains 64 Mg atoms at the 8c site and 32 Si atoms at the 4a site without any point defects. Model 2a is 'Mg₆₄Si₃₂+Mg_i', which contains one additional Mg_i. Models 2b and 2c contain one Mg_i and an O atom at the 4b site (O_i) with different distances between Mg_i and O_i, namely, 'Mg₆₄Si₃₂+Mg_i+O_i'. Model 3a is designated as 'Mg₆₃Si₃₂', i.e., one V_{Mg} exists in a supercell. Models 3b and 3c also contain one V_{Mg} and one O_i with different distances between V_{Mg} and O_i and are expressed as 'Mg₆₃Si₃₂+O_i'. One V_{Si} exists in Model 4a, and one additional O_i exists in Models 4b and 4c; these models are represented as 'Mg₆₄Si₃₁' and 'Mg₆₄Si₃₁+O_i', respectively. Models 3d and 4d are denoted as 'Mg₆₃Si₃₂+O_{Mg}' and 'Mg₆₄Si₃₁+O_{Si}', respectively, where an O atom can be substituted for an Mg/Si atom. We investigated the stability of the point defects in each crystal structure model on the basis of the calculation of total energy E . For the calculation, the E values of Mg, Si, and/or O atoms were added to equalise the number of atoms.

$$E = E(\text{Mg}_{64-a}\text{Si}_{32-b} + c\text{Mg}_i + d\text{O}_i + e\text{O}_{\text{Mg}} + f\text{O}_{\text{Si}}) + (1 + a - c)E(\text{Mg}) + b \cdot E(\text{Si}) + (1 - d - e - f)E(\text{O}), \quad (1)$$

where $a-f$ is a constant (0 or 1). The numbers of k -points in the Brillouin zone for each model, Mg, and Si, were 108, 2028, and 3430, respectively. We also calculated the electronic density of states (DOS) to examine the conduction type. In the KKR method, the generalised gradient approximation and Perdew–Burke–Ernzerhof functional were used. The angular momentum cut-off was 2. The imaginary part added to the Fermi energy was set to

0.0001 Ry to calculate the DOS of Mg_2Si , $\text{Mg}_2\text{Si}_{0.97}$, $\text{Mg}_2\text{Si}_{0.97+0.03\text{O}_{\text{Si}}}$, $\text{Mg}_2\text{Si}_{0.99}$, and $\text{Mg}_2\text{Si}_{0.99+0.01\text{O}_{\text{Si}}}$. The number of k -points was 2168.

The preparation procedure of the Mg_2Si SC that contained V_{Si} and dislocation cores is described elsewhere [17]. The depth profiles of O, carbon (C), hydrogen (H), Si, and MgSi in the prepared Mg_2Si SCs were determined through SIMS (IONTOF, TOF-SIMS5-100) in negative polarity mode. The XPS spectra of the Mg_2Si SC were acquired in a vacuum (1.2×10^{-5} Pa) by using Al $K\alpha$ radiation as a light source (ThermoFisher Scientific, Theta Probe). A cleavage surface was obtained just before the sample was introduced into the XPS chamber. Surface etching was performed in the chamber by using Ar ion milling. Photoelectron holography, a type of atomic resolution holography that can directly reveal a three-dimensional local structure around a target atom [47–63], was performed by using soft X-ray as a light source at the beamline 25SU [64] of the synchrotron radiation facility Super Photon ring-8 GeV (SPring-8), Japan. A wide-angle display-type retarding field analyser was used for the measurement [65]. A cleaved surface was obtained after the introduction of the sample into the vacuum chamber. The vacuum pressure during the measurement was 6.5×10^{-8} Pa. From photoelectron holography, an atomic arrangement of O on W(110) [62] and a defect structure including O at the interface between Al_2O_3 and diamond [63] was revealed. Thus, the position of O in the Mg_2Si SC can be determined if a structure around O has a long-range order.

3. Results and Discussion

By using the FLAPW method, we investigated whether point defects in each supercell were stable or not. Figures S1–S3 show that the E of Models 2a ($\text{Mg}_{64}\text{Si}_{32}+\text{Mg}_{\text{i}}$), 3a ($\text{Mg}_{63}\text{Si}_{32}$), and 4a ($\text{Mg}_{64}\text{Si}_{31}$) were higher than that of Model 1 ($\text{Mg}_{64}\text{Si}_{32}$). This result indicates that the formation energy of Mg_{i} , V_{Mg} , and V_{Si} was positive (+0.197 eV/cell, +0.266 eV/cell, and +0.293 eV/cell, respectively). Consistent with the results of previous studies [34–36], V_{Si} showed the highest E , i.e., it had the highest formation energy, among the point defects. However, Models 2b, 2c, 3b, 3c, 3d, 4b, 4c, and 4d, which all contained O, exhibited a lower E than Model 1, indicating that the introduction of O could stabilise the formation of Mg_{i} , V_{Mg} , and V_{Si} . Models 2c ($\text{Mg}_{64}\text{Si}_{32}+\text{Mg}_{\text{i}}+\text{O}_{\text{i}}$), 3b ($\text{Mg}_{63}\text{Si}_{32}+\text{O}_{\text{i}}$), and 4d ($\text{Mg}_{64}\text{Si}_{31}+\text{O}_{\text{Si}}$) had the lowest E in the cases of Mg_{i} , V_{Mg} , and V_{Si} , respectively. The E values of Models 1, 2a, 3a, 4a, 2c, 3b, and 4d are summarised in Figure 1. Although Model 4a had the highest E , the introduction of O into the Si site (Model 4d) resulted in the lowest E value. The formation energy of $\text{Mg}_{\text{i}}+\text{O}_{\text{i}}$ (Model 2c), $\text{V}_{\text{Mg}}+\text{O}_{\text{i}}$ (Model 3b), and O_{Si} (Model 4d) were -0.272 eV/cell, -0.193 eV/cell, and -0.583 eV/cell, respectively. In addition, the E values of Models 4b and 4c, which contained V_{Si} and O_{i} (see Figure S3), respectively, were lower or equal to those of Models 2c and 3b, which contained $\text{Mg}_{\text{i}}/\text{V}_{\text{Mg}}$ and O_{i} , respectively. The formation energy of $\text{V}_{\text{Si}}+\text{O}_{\text{i}}$ (Models 4b and 4c) was -0.211 eV/cell and -0.296 eV/cell, respectively. In other words, the incorporation of O stabilised the formation of V_{Si} rather than Mg_{i} and V_{Mg} , regardless of whether O was located at the Si site or at the interstitial site. (The formation energy of each defect is summarised in Table S1).

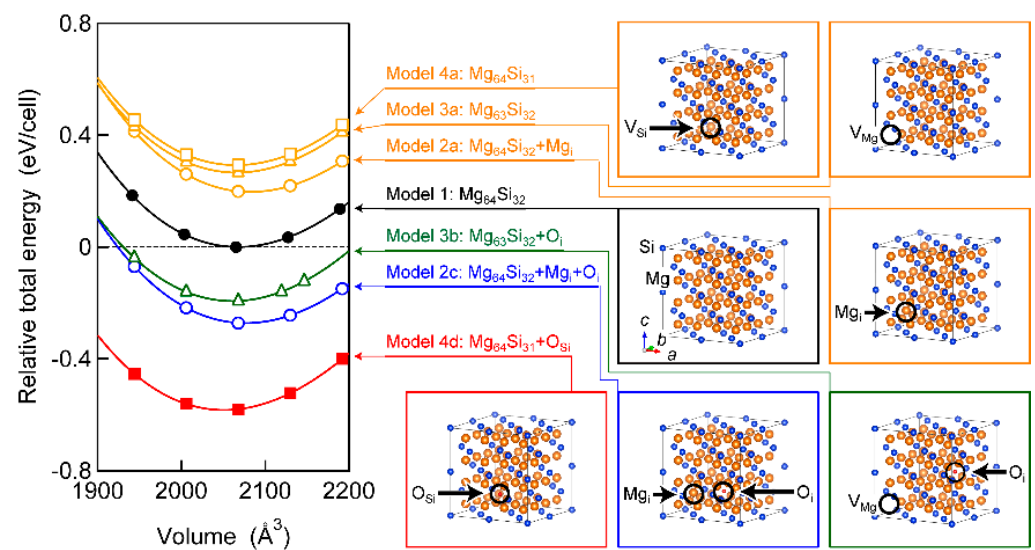


Figure 1. Volume dependence of the total energy of seven crystal structure models relative to the minimum energy of Model 1. Crystal structures were drawn using VESTA [66].

Next, we examined the conduction type of Models 1, 4a, and 4d by calculating their DOS through the FLAPW method. By introducing one V_{Si} defect into $Mg_{64}Si_{32}$, p-type conductivity changed to n-type one (see Figure 2a,b). The band gap increased with the introduction of the V_{Si} defect from 0.11 eV to 0.19 eV. Similar to the introduction of one Mg_i into $Mg_{64}Si_{32}$ and $Mg_{216}Si_{108}$ [21], the substitution of one O for the Si site caused an in-gap state just at the bottom of the conduction band (Figure 2c). Given that the Fermi level (E_F) was located inside the conduction band, $Mg_{64}Si_{31}+O_{Si}$ was found to have n-type conductivity. These calculation results were reproduced using the KKR method, as shown in Figure 2d–f. Note that the fraction of V_{Si} or O_{Si} in the crystal structure models used for the calculation of Figure 2b,c,e,f was approximately 3%. By contrast, the V_{Si} fraction in the prepared Mg_2Si SCs was reported to be approximately 1%. Thus, we calculated the DOS of $Mg_2Si_{0.99}$ by using the KKR method (Figure 2g). The n-type conductivity was confirmed, which was consistent with a previous calculation and used another KKR code [67]. The increase in the band gap was also found in the KKR calculation. The band gap of Mg_2Si was 0.10 eV, whereas that of $Mg_2Si_{0.99}$ and $Mg_2Si_{0.97}$ was 0.15 eV and 0.20 eV, respectively. The band gap of Mg_2Si and $Mg_2Si_{0.97}$ was in good agreement with the FLAPW calculation. For $Mg_2Si_{0.99}+0.01O_{Si}$ (Figure 2h), the in-gap state became smaller than that shown in Figure 2c,f, but E_F continued to exist inside the conduction band. From the above calculations, we found that the presence of V_{Si} or O_{Si} led to n-type conductivity of Mg_2Si . This result was consistent with the experiments showing that the prepared Mg_2Si SCs had a negative Seebeck coefficient, i.e., they had n-type conductivity [17]. Figure 2i presents the lattice constant at the minimum E , which was used for the calculation of the results given in Figure 2a,h. The introduction of V_{Si} or O_{Si} reduced the lattice constant. Experimentally, the smaller lattice constant resulted in an increase in the V_{Si} fraction in Mg_2Si SCs [17]. A similar tendency was reported for the prepared Mg_2Sn SCs, wherein the V_{Mg} fraction increased with the decrease in the lattice constant [16,27]. As expected from the above calculations, O can be O_i or O_{Si} to stabilise V_{Si} if it exists in the crystal lattice of Mg_2Si .

We acquired the depth profiles of O, C, H, Si, and MgSi by using SIMS, as shown in Figure 3, to investigate whether O was present or absent in the Mg_2Si SC. O, C, and H were mainly detected below 200 nm, indicating that the surface of the Mg_2Si SC was contaminated with O, C, and H. As the depth increased to 200 nm, the H intensity decreased to a noise level (<10 counts), and Si and MgSi were clearly detected instead. The C intensity also decreased and reached the noise level at 1600 nm. These results suggested that surface contamination with C and H could be eliminated by etching or cleaving the Mg_2Si SC. On

the other hand, O intensity decreased but remained constant above 1200 nm. Thus, O was expected to exist in the Mg₂Si SC after etching or cleaving.

The presence of O inside the Mg₂Si SC was also confirmed by acquiring the XPS spectra before and after etching, as shown in Figure 4a. C and O peaks, in addition to Mg and Si peaks, were observed before etching. This finding indicated that the surface of the Mg₂Si SC was contaminated and had oxidised. In fact, the surface of Mg₂Si SC is known to oxidise when it is placed in the atmosphere [68]. After etching, the C peak disappeared, but the O peaks remained. Additional detailed information is provided in Figure 4b. Before etching, two peaks were observed in the C 1s XPS spectrum (upper-left figure). These peaks, which were assigned to C-O (290 eV [69]) and C (285 eV), were diminished after etching (lower-left figure). A broad peak consisting of C-O (532 eV), Si-O (532 eV [70]), and Mg-O (530 eV) components were observed in the O 1s XPS spectrum before etching (upper-middle figure). The surface oxidation and/or the presence of O inside the Mg₂Si SC were ascribed to the Si-O and Mg-O components. By etching the surface, the broad O 1s peak changed into double peaks (lower-middle figure) due to a decrease in C-related contamination. In other words, the C-O component at 532 eV disappeared, making the Si-O and Mg-O components more evident after etching. The remaining Si-O and Mg-O components indicated that O existed inside the Mg₂Si SC. The removal of surface oxidation was confirmed by comparing the Mg 2p XPS spectra before and after etching (upper-right and lower-right figures, respectively). A broad peak was observed in the spectra. This peak could be separated into two components at 50 eV and 49 eV. Such components were also found in an Sb-doped Mg₂Si_{0.4}Sn_{0.6} PC and were assigned to the Mg of Mg₂Si (50 eV) and Mg_i (49 eV) components [71]. However, this assignment can be disputed, given the absence of Mg_i in the Mg₂Si SC [17]. Studies [72–74] have reported that the Mg-O and Mg peaks of Mg₂Si components appeared in the Mg 2p XPS spectra at lower and higher binding energies, respectively. In consideration of these studies, as well as the O 1s XPS spectra in this study, we concluded that the components observed at 50 eV and 49 eV were Mg-O and Mg in Mg₂Si components, respectively. Etching the surface changed the intensity ratio of these components. After etching, the Mg-O component decreased, whereas the Mg of the Mg₂Si component increased. This result indicates that although the oxidised surface had been removed, O remained in the Mg₂Si SC.

We further proved that O was present in Mg₂Si SC through the use of photoelectron holography. Figure 5a shows the Mg 2p spectrum (dots), which could be deconvoluted into two components (blue and red curves). The spin-orbit splitting for each component was set at 0.6 eV. In consideration of the XPS results shown previously, we assigned the components at higher and lower binding energies to Mg-O and Mg in Mg₂Si, respectively. The difference in the energy position between the two components was 1 eV and was consistent with that in the Mg 2p XPS spectra. The insets in Figure 5a are the holograms derived from each component (blue-black colour scale). In particular, the hologram for the component at a lower binding energy well coincided with the hologram simulated using the regular atomic arrangement of the Mg and Si atoms of Mg₂Si around an emitter Mg atom (yellow-black colour scale). Thus, the assignment of the components in the Mg 2p spectrum was found to be valid. The Si 2p spectrum (dots) is shown in Figure 5b. The spin-orbit splitting for each component was set at 0.6 eV. Similar to a previous result [68], a component of Si for Mg₂Si at the lowest binding energy and Si-O components at a higher binding energy were present in the Si 2p spectrum (coloured curves). The Si-O components were Si⁺, Si²⁺, Si³⁺, and Si⁴⁺ at 0.5 eV, 0.9 eV, 1.3 eV, and 4.5 eV, respectively. The energy positions of these components were evaluated relative to that of the Si component and were found to correspond reasonably to values in the literature [75–77]. An inset in Figure 5b is an experimental hologram derived from the Si component (left) and a simulated hologram constructed on the basis of the regular atomic arrangement of the Mg and Si atoms of Mg₂Si around an emitter Si atom (right). Given that the experimental hologram coincided with the simulated one, the assignment of the components was confirmed to be valid for the Si 2p spectrum. Although the cleavage surface was prepared in a vacuum, the Mg-O and

Si-O components were found in Mg 2p and Si 2p spectra, respectively, verifying that O was present inside the Mg₂Si SC. The remaining O in an Ar gas and/or the aluminum crucible was used for the preparation of the Mg₂Si SC, which could be a source of O.

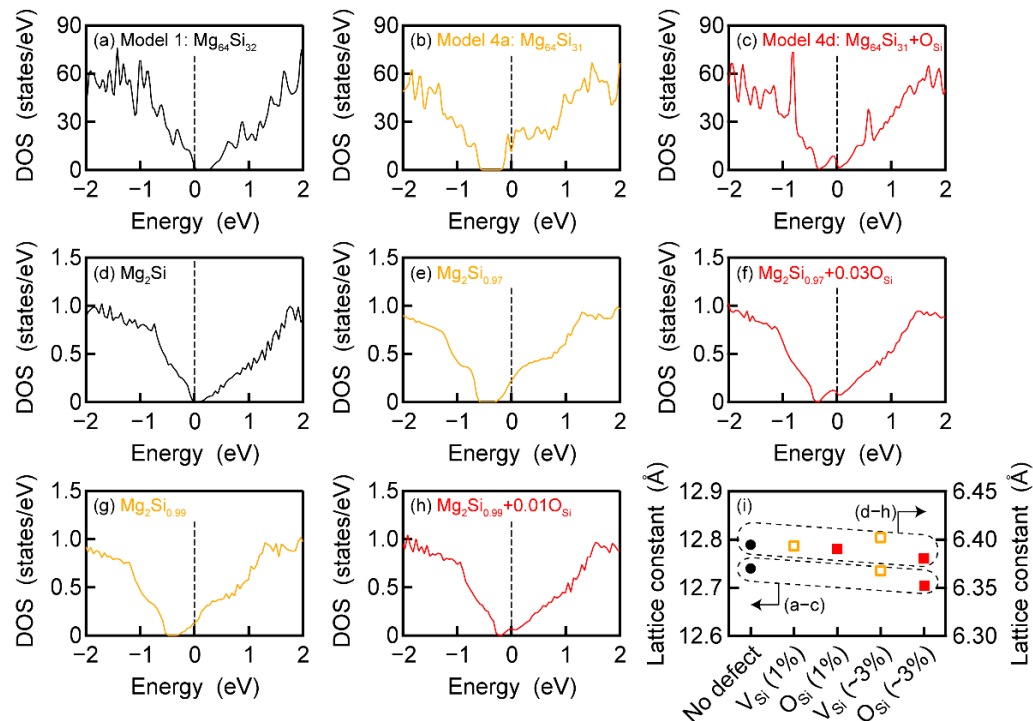


Figure 2. Electronic density of states (DOS) for (a) Model 1, (b) Model 4a, and (c) Model 4d shown in Figure 1. Electronic DOS of the 1 × 1 × 1 cubic cell of (d) Mg₂Si, (e) Mg₂Si_{0.97}, (f) Mg₂Si_{0.97}+0.03O_{Si}, (g) Mg₂Si_{0.99}, and (h) Mg₂Si_{0.99}+0.01O_{Si}. (i) Lattice constant used for the calculation of (a–h), which provided the minimum total energy.

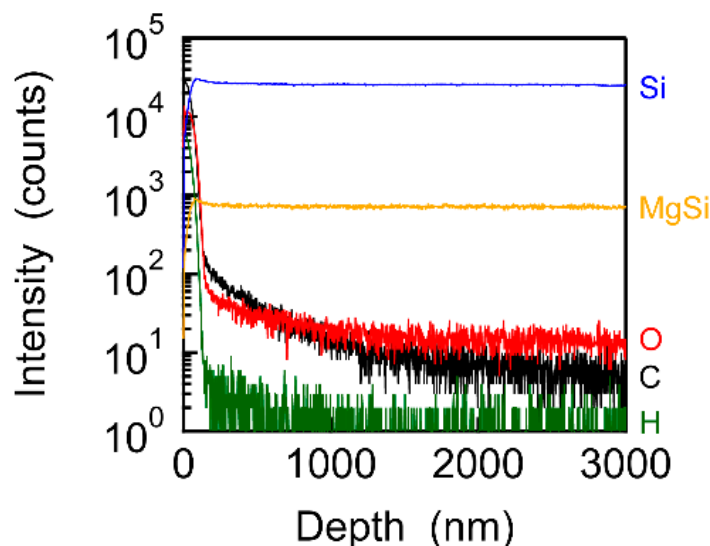


Figure 3. Depth profiles of O, C, H, Si, and MgSi of the Mg₂Si SC.

Here, we discuss the position of O in the Mg₂Si SC. A hologram derived from the Mg-O component is shown in the inset of Figure 5a, which is rather unclear compared with those derived from the Mg and Si components. We reconstructed a simulated hologram of Model 4c (Mg₆₄Si₃₁+O_i) and Model 4d (Mg₆₄Si₃₁+O_{Si}), as shown in Figure 6, to examine the position. The characteristic features in the simulated holograms were not identified

in the experimental hologram. Thus, we could not conclude that O existed at a specific site of the crystal lattice of Mg_2Si . Instead, O was highly likely to be present at the dislocation cores. O was likely diffused and segregated to the dislocation cores during crystal growth. O segregation resulted in the immobilisation of the dislocation cores through the reconstruction of Mg, Si, and O atom locations around the dislocation cores. The reconstruction process reduced the total energy, which, in turn, stabilised V_{Si} . Note that reconstructed atomic arrangements lacked a long-range order; therefore, the hologram derived from the Mg-O component was featureless. In the future, other experiments, such as x-ray absorption spectroscopy and positron annihilation spectroscopy, will be performed to determine the position of O precisely.

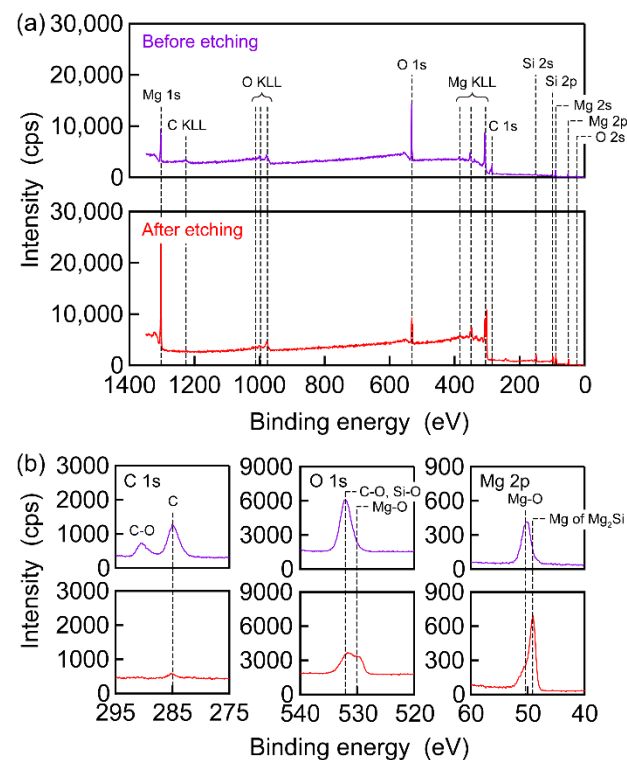


Figure 4. (a) X-ray photoelectron spectroscopy survey spectra and (b) core level spectra of the Mg_2Si SC before and after etching (upper and lower, respectively).

In summary, using the FLAPW and KKR methods, we theoretically predicted that the presence of O stabilised the formation of Mg_i , V_{Mg} , and V_{Si} in Mg_2Si SCs. The formation energy of $V_{\text{Si}}+\text{O}_i$ (Models 4b and 4c) and O_{Si} (Model 4d) was lower or equal to that of the other lattice defects, indicating that Mg_2Si SCs with V_{Si} were stabilised through the incorporation of O. The O_{Si} defect showed the lowest formation energy of the -0.583 eV/cell. The calculated DOS indicated that the electrical conduction of Mg_2Si changed from p-type to n-type by introducing V_{Si} . The n-type conductivity was maintained for the additional introduction of O into Mg_2Si with V_{Si} . The presence of C and O in the prepared Mg_2Si SC was revealed by SIMS and XPS. C existed in the vicinity of the surface of the Mg_2Si SC, whereas O was present not only at the surface but also inside the Mg_2Si SC. The presence of O was also confirmed by photoelectron holography measurements on the cleavage surface of the Mg_2Si SC. In the Mg 2p spectrum, Mg and Mg-O components were observed, which was consistent with the XPS measurements. In the Si 2p spectrum, Si and Si-O components were present. An experimental hologram derived from the Mg and Si components was reproduced by a simulated hologram constructed on the basis of the regular atomic arrangement of the Mg and Si atoms of Mg_2Si around an Mg and Si atom, respectively. On the other hand, an experimental hologram derived from the Mg-O component was featureless and did not coincide with a simulated hologram of Mg_2Si with V_{Si} or O_{Si} . This result

indicated that O could be located at dislocation cores, not at the interstitial site or at the Si site in the Mg_2Si SC. The Mg_2Si SC with V_{Si} may have become stable due to the interaction between O and the dislocation cores. The effect of O as well as the higher preparation temperature of the Mg_2Si SC, are the reasons for the formation of V_{Si} in the Mg_2Si SC.

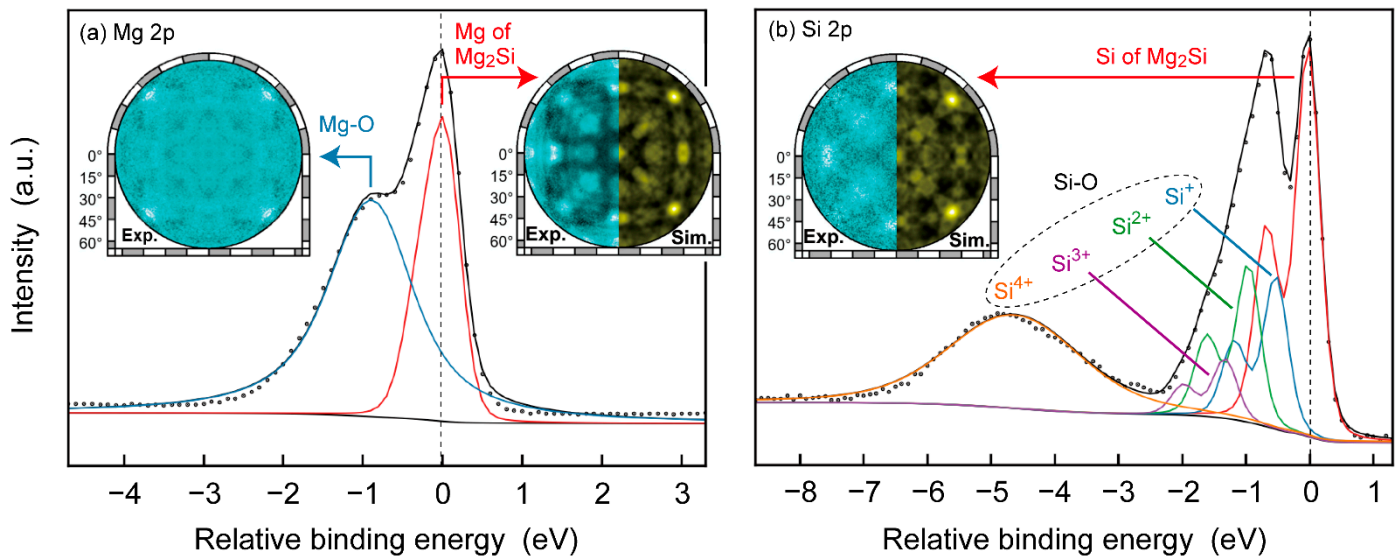


Figure 5. (a) Mg 2p and (b) Si 2p spectra taken in photoelectron holography measurements of the Mg_2Si SC (dots). Each spectrum is deconvoluted into several components (coloured curves). The sum of all components is drawn as a black curve. Insets are holograms derived from measured Mg, Mg-O, and Si components (blue-black colour scale) and simulated holograms (yellow-black colour scale).

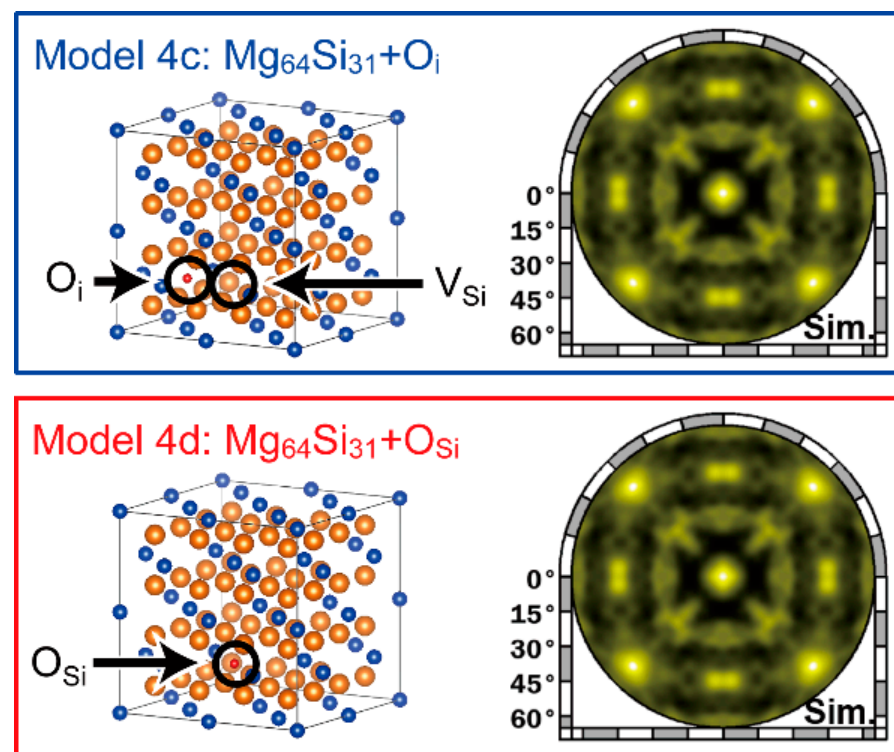


Figure 6. Simulated holograms of Model 4c ($Mg_{64}Si_{31} + O_i$) and Model 4d ($Mg_{64}Si_{31} + O_{Si}$).

Supplementary Materials: The following supporting information can be downloaded at: <https://www.mdpi.com/article/10.3390/nano13071222/s1>, Figure S1: Volume dependence of the total energy for the four crystal structure models relative to the minimum energy of Model 1. Crystal structures are drawn by using VESTA [66]; Figure S2: Volume dependence of the total energy for the five crystal structure models relative to the minimum energy of Model 1; Figure S3: Volume dependence of the total energy for the five crystal structure models relative to the minimum energy of Model 1; Table S1: Formation energy of Mg_i , V_{Mg} , V_{Si} , and their complex defects in combination with O.

Author Contributions: Calculation, K.H. (Kei Hayashi); investigation, K.H. (Kei Hayashi), S.K., Y.H., N.A., Z.H., W.S., K.T. and K.H. (Koichi Hayashi), and T.M.; writing—original draft preparation, K.H. (Kei Hayashi); writing—review and editing, K.H. (Kei Hayashi), T.M., and Y.M.; supervision, K.H. (Kei Hayashi) and Y.M.; funding acquisition, K.H. (Kei Hayashi), K.H. (Koichi Hayashi), and T.M. All authors have read and agreed to the published version of the manuscript.

Funding: This work was partly supported by the Grant-in-Aid for Scientific Research (B) (Grant Nos. 17H03398, 20H01841, 22H02161) and the Grants-in-Aid for Transformative Research Area (A) ‘Hyper-Ordered Structures Science’ (Grant Nos. 20H05878, 20H05881, 20H5882, 20H05884) from the Ministry of Education, Culture, Sports, Science, and Technology of Japan, and was partly based on collaborative research between Sumitomo Metal Mining Co., Ltd. and Tohoku University, which is part of the Vision Co-creation Partnership. The synchrotron radiation experiments were performed with the approval of Japan Synchrotron Radiation Research Institute (JASRI) (Proposal No. 2021A1018).

Data Availability Statement: Not applicable.

Acknowledgments: Kei Hayashi is grateful to R. Shishido from the Institute of Multidisciplinary Research for Advanced Materials, Tohoku University for the SIMS measurement. The authors are also grateful to T. Muro from JASRI for the photoelectron holography measurements.

Conflicts of Interest: The authors declare no conflict of interest.

References

1. Park, J.-S.; Kim, S.; Xie, Z.; Walsh, A. Point defect engineering in thin-film solar cells. *Nat. Rev. Mater.* **2018**, *3*, 194–210. [[CrossRef](#)]
2. Balaraman, A.A.; Dutta, S. Inorganic dielectric materials for energy storage applications: A review. *J. Phys. D Appl. Phys.* **2022**, *55*, 183002. [[CrossRef](#)]
3. Shi, X.-L.; Zou, J.; Chen, Z.-G. Advanced Thermoelectric Design: From Materials and Structures to Devices. *Chem. Rev.* **2020**, *120*, 7399–7515. [[CrossRef](#)] [[PubMed](#)]
4. Liu, W.-S.; Zhang, B.-P.; Li, J.-F.; Zhao, L.-D. Effects of Sb compensation on microstructure, thermoelectric properties and point defect of $CoSb_3$ compound. *J. Phys. D Appl. Phys.* **2007**, *40*, 6784–6790. [[CrossRef](#)]
5. Jiang, G.; He, J.; Zhu, T.; Fu, C.; Liu, X.; Hu, L.; Zhao, X. High Performance $Mg_2(Si,Sn)$ Solid Solutions: A Point Defect Chemistry Approach to Enhancing Thermoelectric Properties. *Adv. Funct. Mater.* **2014**, *24*, 3776–3781. [[CrossRef](#)]
6. Kubouchi, M.; Hayashi, K.; Miyazaki, Y. Quantitative analysis of interstitial Mg in Mg_2Si studied by single crystal X-ray diffraction. *J. Alloys Compd.* **2014**, *617*, 389–392. [[CrossRef](#)]
7. Kubouchi, M.; Ogawa, Y.; Hayashi, K.; Takamatsu, T.; Miyazaki, Y. Effect of Interstitial Mg in $Mg_{2+x}Si$ on Electrical Conductivity and Seebeck Coefficient. *J. Electron. Mater.* **2016**, *45*, 1589–1593. [[CrossRef](#)]
8. Kubouchi, M.; Hayashi, K.; Miyazaki, Y. Electronic structure and thermoelectric properties of boron doped Mg_2Si . *Scr. Mater.* **2016**, *123*, 59–63. [[CrossRef](#)]
9. Tamaki, M.; Sato, H.K.; Kanno, T. Isotropic Conduction Network and Defect Chemistry in $Mg_{3+\delta}Sb_2$ -Based Layered Zintl Compounds with High Thermoelectric Performance. *Adv. Mater.* **2016**, *28*, 10182–10187. [[CrossRef](#)]
10. Hayashi, K.; Eguchi, M.; Miyazaki, Y. Structural and Thermoelectric Properties of Ternary Full-Heusler Alloys. *J. Electron. Mater.* **2017**, *42*, 2710–2716. [[CrossRef](#)]
11. Wu, D.; Wu, L.; He, D.; Zhao, L.-D.; Li, W.; Wu, M.; Jin, M.; Xu, J.; Jiang, J.; Huang, L.; et al. Direct observation of vast off-stoichiometric defects in single crystalline SnSe. *Nano Energy* **2017**, *35*, 321–330. [[CrossRef](#)]
12. Saito, W.; Hayashi, K.; Nagai, H.; Miyazaki, Y. Preparation and thermoelectric properties of mixed valence compound Sn_2S_3 . *JPN J. Appl. Phys.* **2017**, *56*, 061201. [[CrossRef](#)]
13. Hayashibara, Y.; Hayashi, K.; Ando, I.; Kubouchi, M.; Ogawa, Y.; Saito, W.; Miyazaki, Y. Fabrication and Thermoelectric Properties of Al/ Mg_2Si Composite Materials. *Mater. Trans.* **2018**, *59*, 1041–1045. [[CrossRef](#)]
14. Li, H.; Hayashi, K.; Miyazaki, Y. Design and fabrication of full-Heusler compound with positive Seebeck coefficient as a potential thermoelectric material. *Scr. Mater.* **2018**, *150*, 130–133. [[CrossRef](#)]

15. Zhang, Q.; Gu, B.; Wu, Y.; Zhu, T.; Fang, T.; Yang, Y.; Liu, J.; Ye, B.; Zhao, X. Evolution of the Intrinsic Point Defects in Bismuth Telluride-Based Thermoelectric Materials. *ACS Appl. Mater. Interfaces* **2019**, *11*, 41424–41431. [[CrossRef](#)]
16. Saito, W.; Hayashi, K.; Dong, J.; Li, J.-F.; Miyazaki, Y. Control of the Thermoelectric Properties of Mg₂Sn Single Crystals via Point-Defect Engineering. *Sci. Rep.* **2020**, *10*, 2020. [[CrossRef](#)]
17. Hayashi, K.; Saito, W.; Sugimoto, K.; Ohoyama, K.; Hayashi, K.; Happo, N.; Harada, M.; Oikawa, K.; Inamura, Y.; Miyazaki, Y. Preparation, thermoelectric properties, and crystal structure of boron-doped Mg₂Si single crystals. *AIP Adv.* **2020**, *10*, 035115, Erratum in *AIP Adv.* **2021**, *11*, 029903. [[CrossRef](#)]
18. Li, H.; Hayashi, K.; Dong, J.; Li, J.-F.; Miyazaki, Y. Distinct impact of order degree on thermoelectric power factor of p-type full-Heusler Mn₂VAl compounds. *Mater. Res. Express* **2020**, *7*, 055503. [[CrossRef](#)]
19. Huang, Y.; Hayashi, K.; Miyazaki, Y. Electron Conduction Mechanism of Deficient Half-Heusler VFeSb Compound Revealed by Crystal and Electronic Structure Analyses. *Chem. Mater.* **2020**, *32*, 5173–5181. [[CrossRef](#)]
20. Yoshioka, S.; Hayashi, K.; Yokoyama, A.; Saito, W.; Li, H.; Takamatsu, T.; Miyazaki, Y. Crystal structure, electronic structure and thermoelectric properties of β - and γ -Zn₄Sb₃ thermoelectrics: A (3+1)-dimensional superspace group approach. *J. Mater. Chem. C* **2020**, *8*, 9205–9212. [[CrossRef](#)]
21. Hayashi, K.; Miyazaki, Y.; Saito, W.; Kubouchi, M.; Ogawa, Y.; Suzuki, S.; Hayashibara, Y.; Ando, I. Thermoelectric properties of Mg₂Si and its derivatives: Effects of lattice defects and secondary phases. In *Thermoelectric Materials*; Kurosaki, K., Takagiwa, Y., Shi, X., Eds.; De Gruyter: Berlin, Germany, 2020; pp. 99–116.
22. Hayashi, K.; Li, H.; Eguchi, M.; Nagashima, Y.; Miyazaki, Y. Magnetic Full-Heusler Compounds for Thermoelectric Applications. In *Magnetic Materials and Magnetic Levitation*; Sahu, D.R., Ed.; IntechOpen: Rijeka, Croatia, 2020; Chapter 4.
23. Saito, W.; Hayashi, K.; Huang, Z.; Dong, J.; Li, J.-F.; Miyazaki, Y. Enhancing the Thermoelectric Performance of Mg₂Sn Single Crystals via Point Defect Engineering and Sb Doping. *ACS Appl. Mater. Interfaces* **2020**, *12*, 57888–57897. [[CrossRef](#)] [[PubMed](#)]
24. Kanno, T.; Tamaki, H.; Yoshiya, M.; Uchiyama, H.; Maki, S.; Takata, M.; Miyazaki, Y. High-Density Frenkel Defects as Origin of N-Type Thermoelectric Performance and Low Thermal Conductivity in Mg₃Sb₂-Based Materials. *Adv. Funct. Mater.* **2021**, *31*, 2008469. [[CrossRef](#)]
25. Li, H.; Hayashi, K.; Nagashima, Y.; Yoshioka, S.; Dong, J.; Li, J.-F.; Miyazaki, Y. Effects of Disorder on the Electronic Structure and Thermoelectric Properties of an Inverse Full-Heusler Mn₂CoAl Alloy. *Chem. Mater.* **2021**, *33*, 2543–2547. [[CrossRef](#)]
26. Yoshioka, S.; Hayashi, K.; Yokoyama, A.; Saito, W.; Miyazaki, Y. Crystal structure, microstructure, and electronic transport properties of β -Zn₄Sb₃ thermoelectrics: Effects of Zn intercalation and deintercalation. *Mater. Today Energy* **2021**, *21*, 100723. [[CrossRef](#)]
27. Saito, W.; Hayashi, K.; Huang, Z.; Sugimoto, K.; Ohoyama, K.; Happo, N.; Harada, M.; Oikawa, K.; Inamura, Y.; Hayashi, K.; et al. Chemical-Pressure-Induced Point Defects Enable Low Thermal Conductivity for Mg₂Sn and Mg₂Si Single Crystals. *ACS Appl. Energy Mater.* **2021**, *4*, 5123–5131. [[CrossRef](#)]
28. Huang, Y.; Hayashi, K.; Miyazaki, Y. Outstanding thermoelectric performance of n-type half-Heusler V(Fe_{1-x}Co_x)Sb compounds at room-temperature. *Acta Mater.* **2021**, *215*, 117022. [[CrossRef](#)]
29. Huang, Z.; Hayashi, K.; Saito, W.; Miyazaki, Y. Realizing p-type Mg₂Sn Thermoelectrics via Ga-Doping and Point Defect Engineering. *ACS Appl. Energy Mater.* **2021**, *4*, 13044–13050. [[CrossRef](#)]
30. Hayashi, K. Enhancement of thermoelectric performance of Mg₂Sn single crystals via lattice-defect engineering. *JSAP Rev.* **2022**, *2022*, 220403.
31. Huang, Z.; Hayashi, K.; Saito, W.; Pei, J.; Li, J.-F.; Miyazaki, Y. Enhanced Thermoelectric Performance of p-type Mg₂Sn Single Crystals via Multi-scale Defect Engineering. *J. Mater. Chem. A* **2023**, *11*, 2652–2660. [[CrossRef](#)]
32. Ning, H.; Mastrotillo, G.D.; Grasso, S.; Du, B.; Mori, T.; Hu, C.; Xu, Y.; Simpson, K.; Maizza, G.; Reece, M.J. Enhanced thermoelectric performance of porous magnesium tin silicide prepared using pressure-less spark plasma sintering. *J. Mater. Chem. A* **2015**, *3*, 17426–17432. [[CrossRef](#)]
33. Gao, P.; Davis, J.D.; Poltavets, V.V.; Hogan, T.P. The p-type Mg₂Li_xSi_{0.4}Sn_{0.6} thermoelectric materials synthesized by a B₂O₃ encapsulation method using Li₂CO₃ as the doping agent. *J. Mater. Chem. C* **2016**, *4*, 929–934. [[CrossRef](#)]
34. Kato, A.; Yagi, T.; Fukusako, N. First-principles studies of intrinsic point defects in magnesium silicide. *J. Phys. Condens. Matter* **2009**, *21*, 205801. [[CrossRef](#)]
35. Jund, P.; Viennois, R.; Colinet, C.; Hug, G.; Fèvre, M.; Tédénac, J.-C. Lattice stability and formation energies of intrinsic defects in Mg₂Si and Mg₂Ge via first principles simulations. *J. Phys. Condens. Matter* **2013**, *25*, 035403. [[CrossRef](#)]
36. Liu, X.; Xi, L.; Qiu, W.; Yang, J.; Zhu, T.; Zhao, X.; Zhang, W. Significant roles of intrinsic point defects in Mg₂X (X = Si, Ge, Sn) thermoelectric materials. *Adv. Electron. Mater.* **2016**, *2*, 1500284. [[CrossRef](#)]
37. Farahi, N.; Prabhudev, S.; Botton, G.A.; Zhao, J.; Tse, J.S.; Liu, Z.; Salvador, J.R.; Kleinke, H. Local structure and thermoelectric properties of Mg₂Si_{0.977-x}Ge_xBi_{0.023} (0.1 ≤ x ≤ 0.4). *J. Alloys Compd.* **2015**, *644*, 249–255. [[CrossRef](#)]
38. Imai, Y.; Sohma, M.; Suemasu, T. Effect of oxygen incorporation in the Mg₂Si lattice on its conductivity type—A possible reason of the p-type conductivity of postannealed Mg₂Si thin film. *J. Alloys Compd.* **2016**, *676*, 91–95. [[CrossRef](#)]
39. Kurokawa, M.; Shimizu, T.; Uehara, M.; Katagiri, A.; Akiyama, K.; Matsushima, M.; Uchida, H.; Kimura, Y.; Funakubo, H. Control of p- and n-type Conduction in Thermoelectric Non-doped Mg₂Si Thin Films Prepared by Sputtering Method. *MRS Adv.* **2018**, *3*, 1355–1359. [[CrossRef](#)]
40. Möller, H.J. The movement of dissociated dislocations in the diamond-cubic structure. *Acta Metall.* **1978**, *26*, 963–973. [[CrossRef](#)]

41. Umerski, A.; Jones, R. The interaction of oxygen with dislocation cores in silicon. *Philos. Mag. A* **1993**, *67*, 905–915. [[CrossRef](#)]
42. Yonenaga, I.; Sumino, K. Influence of oxygen precipitation along dislocations on the strength of silicon crystals. *J. Appl. Phys.* **1996**, *80*, 734–738. [[CrossRef](#)]
43. Ide, T.; Harada, H.; Miyamura, Y.; Imai, M.; Nakano, S.; Kakimoto, K. Relationship between Dislocation Density and Oxygen Concentration in Silicon Crystals during Directional Solidification. *Crystals* **2018**, *8*, 244. [[CrossRef](#)]
44. Blaha, P.; Schwarz, K.; Madsen, G.; Kvasnicka, D.; Luitz, J. *WIEN2k, An Augmented Plane Wave + Local Orbitals Program for Calculating Crystal Properties*; Schwarz, K., Ed.; Techn. Universität Wien: Wien, Austria, 2001.
45. AkaiKKR Machikaneyama, Ab-Initio Electronic-Structure Calculation Code. Available online: <http://kkri.ssp.u-tokyo.ac.jp/> (accessed on 6 October 2022).
46. Shi, G.; Kioupakis, E. Relativistic quasiparticle band structures of Mg₂Si, Mg₂Ge, and Mg₂Sn: Consistent parameterization and prediction of Seebeck coefficients. *J. Appl. Phys.* **2018**, *123*, 085114. [[CrossRef](#)]
47. Szöke, A. X-ray and electron holography using a local reference beam. *AIP Conf. Proc.* **1986**, *147*, 361–367.
48. Matsushita, T.; Yoshigoe, A.; Agui, A. Electron holography: A maximum entropy reconstruction scheme. *Europhys. Lett.* **2005**, *71*, 597–603. [[CrossRef](#)]
49. Matsushita, T.; Guo, F.Z.; Matsui, F.; Kato, Y.; Daimon, H. Three-dimensional atomic-arrangement reconstruction from an Auger-electron hologram. *Phys. Rev. B* **2007**, *75*, 085419. [[CrossRef](#)]
50. Matsushita, T.; Guo, F.Z.; Suzuki, M.; Matsui, F.; Daimon, H.; Hayashi, K. Reconstruction algorithm for atomic-resolution holography using translational symmetry. *Phys. Rev. B* **2008**, *78*, 144111. [[CrossRef](#)]
51. Matsushita, T.; Matsui, F.; Daimon, H.; Hayashi, K. Photoelectron holography with improved image reconstruction. *J. Electron Spectrosc. Relat. Phenom.* **2010**, *178–179*, 195–200. [[CrossRef](#)]
52. Matsui, H.; Matsui, F.; Maejima, N.; Matsushita, T.; Daimon, H. Stacking registry determination of graphene grown on the SiC(0001) by photoelectron holography. *Surf. Sci.* **2015**, *635*, 1–4. [[CrossRef](#)]
53. Matsui, F.; Eguchi, R.; Nishiyama, S.; Izumi, M.; Uesugi, E.; Goto, H.; Matsushita, T.; Sugita, K.; Daimon, H.; Hamamoto, Y.; et al. Photoelectron Holographic Atomic Arrangement Imaging of Cleaved Bimetal-intercalated Graphite Superconductor Surface. *Sci. Rep.* **2016**, *6*, 36258. [[CrossRef](#)]
54. Fukami, S.; Taguchi, M.; Adachi, Y.; Sakaguchi, I.; Watanabe, K.; Kinoshita, T.; Muro, T.; Matsushita, T.; Matsui, F.; Daimon, H.; et al. Correlation Between High Gas Sensitivity and Dopant Structure in W-doped ZnO. *Phys. Rev. Appl.* **2017**, *7*, 064029. [[CrossRef](#)]
55. Tsutsui, K.; Matsushita, T.; Natori, K.; Muro, T.; Morikawa, Y.; Hoshii, T.; Kakushima, K.; Wakabayashi, H.; Hayashi, K.; Matsui, F.; et al. Individual Atomic Imaging of Multiple Dopant Sites in As-Doped Si Using Spectro-Photoelectron Holography. *Nano Lett.* **2017**, *17*, 7533–7538. [[CrossRef](#)]
56. Matsushita, T. Algorithm for Atomic Resolution Holography Using Modified L₁-Regularized Linear Regression and Steepest Descent Method. *Phys. Status Solidi B* **2018**, *255*, 1800091. [[CrossRef](#)]
57. Yokoya, T.; Terashima, K.; Takeda, A.; Fukura, T.; Fujiwara, H.; Muro, T.; Kinoshita, T.; Kato, H.; Yamasaki, S.; Oguchi, T.; et al. Asymmetric Phosphorus Incorporation in Homoepitaxial P-Doped (111) Diamond Revealed by Photoelectron Holography. *Nano Lett.* **2019**, *19*, 5915–5919. [[CrossRef](#)]
58. Yamamoto, Y.; Ang, A.K.R.; Kimura, K.; Matsushita, T.; Hirose, Y.; Oka, D.; Hayashi, K. Anion arrangement analysis of oxynitride perovskite thin film with inverse photoelectron holography. *J. Electron Spectrosc. Relat. Phenom.* **2021**, *246*, 147018. [[CrossRef](#)]
59. Tang, J.; Takeuchi, S.; Tanaka, M.; Tomita, H.; Hashimoto, Y.; Nagata, T.; Chen, J.; Ohkochi, T.; Kotani, Y.; Matsushita, T.; et al. Direct Observation of Atomic Structures and Chemical States of Active and Inactive Dopant Sites in Mg-Doped GaN. *ACS Appl. Electron. Mater.* **2022**, *4*, 4719–4723. [[CrossRef](#)]
60. Uenuma, M.; Kuwaharada, S.; Tomita, H.; Tanaka, M.; Sun, Z.; Hashimoto, Y.; Fujii, M.N.; Matsushita, T.; Uraoka, Y. Atomic structure analysis of gallium oxide at the Al₂O₃/GaN interface using photoelectron holography. *Appl. Phys. Express* **2022**, *15*, 085501. [[CrossRef](#)]
61. Li, Y.; Sun, Z.; Kataoka, N.; Setoguchi, T.; Hashimoto, Y.; Takeuchi, S.; Koga, S.; Muro, T.; Demura, S.; Noguchi, K.; et al. Incorporation Site and Valence State of Sn Atoms in Sn-Substituted La(O,F)BiS₂ Superconductor. *J. Phys. Soc. Jpn.* **2022**, *91*, 054602. [[CrossRef](#)]
62. Takeuchi, S.; Hashimoto, Y.; Daimon, H.; Matsushita, T. High-precision atomic image reconstruction from photoelectron hologram of O on W(110) by SPEA-L1. *J. Electron Spectrosc. Relat. Phenom.* **2022**, *256*, 147177. [[CrossRef](#)]
63. Fujii, M.N.; Tanaka, M.; Tsuno, T.; Hashimoto, Y.; Tomita, H.; Takeuchi, S.; Koga, S.; Sun, Z.; Enriquez, J.I.; Morikawa, Y.; et al. Atomic Imaging of Interface Defects in an Insulating Film on Diamond. *Nano Lett.* **2023**, *23*, 1189–1194. [[CrossRef](#)]
64. Senba, Y.; Ohashi, H.; Kotani, Y.; Nakamura, T.; Muro, T.; Ohkochi, T.; Tsuji, N.; Kishimoto, H.; Miura, T.; Tanaka, M.; et al. Upgrade of beamline BL25SU for soft x-ray imaging and spectroscopy of solid using nano- and micro-focused beams at SPring-8. *AIP Conf. Proc.* **2016**, *1741*, 030044.
65. Muro, T.; Ohkochi, T.; Kato, Y.; Izumi, Y.; Fukami, S.; Fujiwara, H.; Matsushita, T. Wide-angle display-type retarding field analyzer with high energy and angular resolutions. *Rev. Sci. Instrum.* **2017**, *88*, 123106. [[CrossRef](#)] [[PubMed](#)]
66. Momma, K.; Izumi, F. VESTA 3 for three-dimensional visualization of crystal, volumetric and morphology data. *J. Appl. Crystallogr.* **2011**, *44*, 1272–1276. [[CrossRef](#)]

67. Zwolenski, P.; Tobola, J.; Kaprzyk, S. KKR-CPA study of electronic structure and relative stability of Mg_2X ($X = Si, Ge, Sn$) thermoelectrics containing point defects. *J. Alloys Compd.* **2015**, *627*, 85–90. [[CrossRef](#)]
68. Esaka, F.; Nojima, T.; Udono, H.; Magara, M.; Yamamoto, H. Non-destructive depth analysis of the surface oxide layer on Mg_2Si with XPS and XAS. *Surf. Interface Anal.* **2016**, *48*, 432–435. [[CrossRef](#)]
69. Shchukarev, A.V.; Korolkov, D.V. XPS study of group IA carbonates. *Cent. Eur. J. Chem.* **2004**, *2*, 347–362. [[CrossRef](#)]
70. Beamson, G.; Briggs, D. *High Resolution XPS of Organic Polymers—The Scienta ESCA300 Database*; Wiley Interscience: New York, NY, USA, 1992.
71. Du, Z.; Zhu, T.; Chen, Y.; He, J.; Gao, H.; Jiang, G.; Tritt, T.M.; Zhao, X. Roles of interstitial Mg in improving thermoelectric properties of Sb-doped $Mg_2Si_{0.4}Sn_{0.6}$ solid solutions. *J. Mater. Chem.* **2012**, *22*, 6838–6844. [[CrossRef](#)]
72. Sekino, K.; Midonoya, M.; Udono, H.; Yamada, Y. Preparation of Schottky contacts on n-type Mg_2Si single crystalline substrate. *Phys. Proc.* **2011**, *11*, 171–173. [[CrossRef](#)]
73. Liao, Y.; Xie, J.; Lv, B.; Xiao, Q.; Xie, Q. X-ray photoelectron spectroscopy characterization of band offsets of MgO/Mg_2Si and SiO_2/Mg_2Si heterojunctions. *Surf. Interface Anal.* **2021**, *53*, 852–859. [[CrossRef](#)]
74. Liao, Y.; Xie, J.; Lv, B.; Xiao, Q.; Xie, Q. The Degradation Mechanism of Mg_2Si during Exploitation at High Temperature. *Phys. Status Solidi* **2021**, *258*, 2100425. [[CrossRef](#)]
75. Alfonsetti, R.; De Simone, G.; Lozzi, L.; Passacantando, M.; Picozzi, P.; Santucci, S. SiO_x Surface Stoichiometry by XPS: A Comparison of Various Methods. *Surf. Interface Anal.* **1994**, *22*, 89–92. [[CrossRef](#)]
76. Raider, S.I.; Fritsch, R. Silicon Monoxide Thin Films. *J. Electrochem. Soc.* **1976**, *123*, 1754–1757. [[CrossRef](#)]
77. Nguyen, T.P.; Lefrant, S. XPS study of SiO thin films and SiO -metal interfaces. *J. Phys. Condens. Matter* **1989**, *1*, 5197–5204. [[CrossRef](#)]

Disclaimer/Publisher’s Note: The statements, opinions and data contained in all publications are solely those of the individual author(s) and contributor(s) and not of MDPI and/or the editor(s). MDPI and/or the editor(s) disclaim responsibility for any injury to people or property resulting from any ideas, methods, instructions or products referred to in the content.